Research Square

Preprints are preliminary reports that have not undergone peer review.
They should not be considered conclusive, used to inform clinical practice,
or referenced by the media as validated information.

Integrated Geomechanically and Acid Fracturing Approach for Optimizing Treatment Design in Carbonate Reservoirs: A Case Study from Southwest Iran

Mohammad Mirhashemi
Petroleum University of Technology
sadegh Saffarzadeh Hosseini
saffarzadeh@put.ac.ir

Petroleum University of Technology

Research Article

Keywords: Acid fracturing, Geomechanically modeling, Carbonate reservoir, Production optimization, GOHFER, PIPESIM, Fracture permeability

Posted Date: June 18th, 2026

DOI: https://doi.org/10.21203/rs.3.rs-9986398/v1

License: This work is licensed under a Creative Commons Attribution 4.0 International License.
Read Full License

Additional Declarations: No competing interests reported.

Integrated Geomechanically and Acid Fracturing Approach for Optimizing Treatment Design in Carbonate Reservoirs: A Case Study from Southwest Iran

Mohammad Mirhashemi[a], Sadegh Saffarzadeh Hosseini[a],

[a] Department of Petroleum Engineering, Abadan Faculty of Petroleum, Petroleum University of Technology, Abadan, Iran

Abstract

Hydraulic fracturing in deep carbonate reservoirs requires accurate prediction of fracture geometry and conductivity, particularly when acid fracturing is applied without proppant support. This study develops and implements a fully coupled numerical workflow to simulate acid fracturing treatments under field-representative conditions in the Bangestan reservoir (Ilam and Sarvak formations). The model integrates wellbore geometry, geomechanical properties, non-Newtonian fluid rheology, leak-off mechanisms, and pumping schedules within an adaptive time-stepping framework using GOHFER software. Prior to main simulations, the 1D geomechanical model was calibrated using field XLOT test data, ensuring reliable estimation of in-situ stresses and rock mechanical properties. A critical component of this work is the systematic selection of the optimal stimulation zone based on simultaneous evaluation of static and dynamic rock mechanical behavior and petrophysical parameters. Among evaluated intervals, Zones 6.1 and 6.2 were identified as the most suitable candidates, exhibiting low elastic moduli (below 30 GPa), reduced brittleness, increased oil saturation, and favorable stress regimes. Additionally, a wellbore-centric recovery enhancement method was implemented, which eliminated bottomhole pressure drop and enabled optimized production. Importantly, the appropriate completion string must be re-optimized for each specific acid fracturing outcome, depending on the resulting fracture geometry. This comprehensive optimization significantly increased wellhead pressure, allowing natural fluid transfer from the wellhead to the surface facility without any downhole pump (e.g., ESP or rod pump). Sensitivity analyses revealed optimal injection conditions at 22 bbl/min for fracture width and 17 bbl/min for fracture length, with injected volumes of 90,000 gal and 81,000 gal, respectively. Nodal analysis using PIPESIM demonstrated that increasing tubing diameter from 2.5 to 6 inches improves production capacity by 60–70%, confirming wellbore hydraulics as the dominant limiting factor. The fully coupled geomechanical-hydraulic framework proved essential for capturing stress redistribution and fracture containment. Despite uncertainties in static-dynamic modulus conversion, the proposed workflow offers a robust, field-applicable methodology for optimizing acid fracture design in mechanically heterogeneous carbonate reservoirs.

Key Words: Acid fracturing, Geomechanically modeling, Carbonate reservoir, Production optimization, GOHFER, PIPESIM, Fracture permeability.

1. Introduction

Hydraulic fracturing has become one of the most critical stimulation techniques for enhancing productivity in low-permeability and unconventional reservoirs. As reservoir targets move toward deeper, tighter, and more geomechanically complex formations, the accurate prediction of fracture initiation, propagation, and post-treatment conductivity has become increasingly important. The efficiency of a stimulation treatment is governed by the coupled interaction between wellbore geometry, in-situ stresses, rock mechanical properties, fluid rheology, proppant transport, and operational constraints. Therefore, a comprehensive and fully coupled numerical modeling framework is essential for reliable design and performance evaluation.

Fracture propagation is a highly nonlinear and transient process controlled by stress redistribution around the wellbore, elastic deformation of the formation, fluid flow within the fracture, leak-off into the porous matrix, and, when applicable, proppant transport and settling. Small variations in mechanical properties, fluid characteristics, or pumping schedules can lead to significant differences in fracture geometry and conductivity. Consequently, simplified analytical approaches are often insufficient for representing field-scale treatments, particularly in heterogeneous or layered reservoirs. In carbonate reservoirs specifically, acid fracturing presents additional complexities due to the reactive nature of the fluid, which creates conductivity through differential etching rather than proppant placement.

In recent years, advances in computational methods and reservoir characterization techniques have enabled more rigorous numerical simulation of hydraulic fracturing treatments. Fully coupled models that integrate geomechanics, fluid flow, heat transfer, and proppant transport provide a more realistic representation of fracture evolution and closure behavior. However, the reliability of such simulations strongly depends on the accuracy and consistency of input data, including well trajectory information, completion details, rock mechanical properties, fluid rheology parameters, leak-off characteristics, and operational pumping schedules. Despite these advances, most existing coupled models focus on proppant-based fracturing in clastic reservoirs, leaving a gap in validated workflows for acid fracturing in carbonate formations where geomechanical heterogeneity strongly influences etching patterns and final conductivity.

The objective of this study is to develop and implement a comprehensive numerical workflow for simulating hydraulic fracturing treatments under field-representative conditions. The modeling approach integrates detailed wellbore geometry, reservoir geomechanical properties, non-Newtonian fluid behavior, fluid loss mechanisms, proppant transport dynamics, and time-dependent pumping schedules within a fully coupled time-stepping framework. By systematically defining and calibrating these parameters, the model aims to provide realistic predictions of fracture geometry, pressure evolution, proppant distribution, and post-closure conductivity.

The outcomes of this work contribute to improved treatment design optimization, better understanding of fracture growth dynamics, and enhanced prediction of well performance. The proposed methodology can be applied to a wide range of reservoirs and operational scenarios, offering a structured and technically rigorous framework for advanced hydraulic fracturing simulation and evaluation.

2. Literature review

Early theoretical foundations of hydraulic fracturing mechanics were established by developing analytical solutions for pressurized crack propagation in elastic media. This work clarified the relationship between injection rate, fluid viscosity, and fracture geometry, forming the basis of later design models (Perkins and Kern, 1970). Building upon linear elastic fracture mechanics, a viscosity-dominated fracture growth regime

was identified, introducing dimensionless scaling parameters that distinguished toughness- and viscosity-controlled propagation. These formulations became central to early fracture design charts (Nordgren, 1972). A revised fracture width prediction methodology was proposed by incorporating fluid leak-off behavior into planar fracture models. The study improved estimation of fracture aperture evolution during pumping (Daneshy, 1973). Experimental observations in laboratory blocks provided validation for two-dimensional fracture propagation assumptions. The results demonstrated reasonable agreement between analytical solutions and controlled injection tests (Cleary, 1978).

Field-scale hydraulic fracturing monitoring in tight gas formations revealed that fracture height growth is strongly influenced by stress contrasts between layers. These findings led to improved layered-reservoir fracture containment models (Warpinski et al., 1982). A comprehensive fracture design framework integrating rock mechanics, fluid rheology, and leak-off was introduced. The methodology standardized treatment evaluation practices across the industry (Economides and Nolte, 1984).

The transition from 2D to 3D fracture modeling (e.g., Crouch and Starfield, 1990) marked a significant leap in accuracy, yet these models remained computationally expensive and often lacked coupling with fluid flow. Laboratory-scale proppant transport experiments in slot models demonstrated non-uniform settling behavior and near-wellbore proppant banking, challenging earlier uniform placement assumptions (Clark, 1992). Subsequent analytical studies refined proppant settling criteria in shear-thinning fluids, establishing relationships between rheology and suspension stability (Shah, 1993). Detailed fracture conductivity testing under closure stress quantified permeability degradation due to proppant crushing and embedment, providing improved post-fracture production forecasts (Penny, 1994). Advancements in multi-layer fracture simulators enabled evaluation of stress barriers and interfacial mechanical contrasts. The results showed that modest stress differences can significantly limit vertical growth (Daneshy, 1998). Scaling laws governing fracture propagation regimes were rigorously reformulated using dimensionless analysis. These results clarified transitions between toughness- and viscosity-dominated growth (Valkó and Economides, 1999).

A fully coupled poroelastic hydraulic fracturing formulation demonstrated that pore pressure diffusion can delay fracture closure and modify effective stress distribution (Adachi et al., 2002). Attention then shifted toward complex fracture networks, where numerical simulations indicated that natural fractures may promote branching under low stress anisotropy conditions (Renshaw and Pollard, 2004). Comparative evaluation of pseudo-3D and planar 3D fracture simulators highlighted limitations in simplified height-growth assumptions and encouraged adoption of fully three-dimensional approaches (Settari and Cleary, 2006). A transient fracture growth model incorporating time-dependent leak-off behavior confirmed deviations from classical Carter leak-off under tight formation conditions (Detournay, 2007). Acid fracturing simulations in carbonate formations revealed that dissolution kinetics significantly influence etched fracture conductivity and long-term productivity (Economides et al., 2008). Microseismical monitoring studies provided field-scale evidence of asymmetric fracture growth caused by stress anisotropy and natural fracture interaction (Maxwell et al., 2009). Height containment modeling in layered reservoirs was further refined through field validation, confirming the dominant role of stress contrast and mechanical layering (Warpinski et al., 2009). Investigations into fracture conductivity degradation due to fines migration quantified long-term productivity loss mechanisms in tight formations (Gupta et al., 2010).

An integrated geomechanics–reservoir simulator demonstrated improved production forecasting accuracy in tight gas systems by accounting for stress-dependent permeability (Fisher et al., 2011). Shale brittleness indices derived from mineralogical analysis were correlated with fracture complexity, offering a design parameter for unconventional reservoirs (Rickman et al., 2011). Stress shadow modeling in multi-cluster

horizontal wells revealed reduced cluster efficiency at small spacing intervals (Williams et al., 2012). Slick water fracturing experiments showed significant proppant banking near the wellbore, emphasizing the importance of transport modeling in low-viscosity systems (Evans et al., 2013). Non-isothermal hydraulic fracturing simulations confirmed that thermal stresses can alter fracture geometry, particularly in high-temperature reservoirs (Huang et al., 2014). Laboratory investigations under high-pressure conditions demonstrated deviations from classical leak-off assumptions in ultra-tight formations (Anderson et al., 2014). Field implementation of zipper fracturing showed enhanced fracture complexity due to inter-well stress interference (Roberts et al., 2015). Rough fracture surface modeling improved prediction of residual fracture width after closure, highlighting the importance of surface asperities (Lee et al., 2016). Mineralogical control on fracture toughness variability in shale formations was quantified, showing strong dependence on quartz content (Mahmoud et al., 2016). Refracturing simulations demonstrated stress reorientation effects and the potential for secondary fracture network creation (Jackson et al., 2017). Experimental validation of shear-thinning fluid rheology effects on proppant settling confirmed improved suspension performance at high consistency indices (Nouri et al., 2018). Height growth modeling in stratified formations emphasized the combined effect of stress contrast and elastic modulus variation (Silva et al., 2018). Production data analysis from optimized multi-stage fracturing indicated improved estimated ultimate recovery (EUR) through cluster spacing optimization (Brown et al., 2019). Microseismical-based fracture mapping confirmed complex, non-planar fracture growth patterns in anisotropic stress fields (Kim et al., 2019).

Coupled acid-fracture propagation models revealed that reaction kinetics and temperature strongly control etched fracture width (Hassan et al., 2020). Perforation phasing studies demonstrated measurable influence on breakdown pressure and fracture initiation orientation (Lopez et al., 2020). Non-Darcy flow effects within fractures were quantified numerically, showing elevated pressure gradients at high injection rates (Wang et al., 2021). Proppant crushing experiments at ultra-high closure stresses confirmed the superior mechanical integrity of ceramic materials compared to natural sand (Peterson et al., 2021). Three-dimensional proppant transport simulations revealed non-uniform vertical placement and gravitational segregation effects (Yousef and Ahmed, 2022). Stress-dependent fracture conductivity correlations were experimentally validated under cyclic loading conditions (Garcia et al., 2022). Comparative fracture modeling approaches demonstrated that complex fracture network simulations better reproduce field microseismic patterns than planar models (Thompson and Li, 2023).

A fully coupled poroelastic hydraulic fracturing model was developed that demonstrated pore pressure diffusion delays fracture closure and modifies effective stress distribution, with numerical simulations providing accurate predictions of fracture geometry in permeable formations, although high computational cost remained a challenge for field-scale applications (Adachi et al., 2007).

The Analytic Hierarchy Process was applied to improve human performance in industrial decision-making, and the multi-criteria model successfully prioritized competing operational factors in complex engineering environments, but the subjective nature of pairwise comparisons introduced potential bias requiring careful calibration (Albayrak and Erensal, 2004).

A new fracability index was developed for identifying hydraulic fracturing candidate zones in carbonate reservoirs that integrated rock mechanical properties, brittleness, and natural fracture density, successfully ranking optimal stimulation intervals, although validating the index across different reservoir lithologies and stress regimes remained a challenge (Amiri et al., 2021).

A combined AHP-Goal Programming model was proposed for quality control systems in manufacturing, and the integrated approach effectively balanced multiple conflicting objectives including cost, quality, and

production efficiency, but the complexity of model calibration and parameter sensitivity limited broader industrial adoption (Badri, 2001).
Boundary element methods were advanced for solid mechanics applications enabling more accurate three-dimensional fracture modeling, and the numerical framework reduced computational effort compared to finite element methods for certain fracture problems, however handling non-linear material behavior and complex fracture interaction geometries remained a challenge (Crouch and Starfield, 1990).
A three-dimensional numerical model was developed to describe acid fracture conductivity in carbonate formations, and the coupled reactive flow-geomechanics approach successfully predicted etched fracture width and conductivity distribution, but accurately representing heterogeneous reaction kinetics and wormhole formation near the fracture face remained a significant challenge (Mirhashemi et al., 2023).
Numerical simulations of fracture propagation in naturally fractured rock masses demonstrated that pre-existing natural fractures promote branching under low stress anisotropy conditions, and the results explained complex fracture network geometries observed in field microseismic data, although the assumption of idealized fracture geometries and simplified interaction criteria presented a key limitation (Renshaw and Pollard, 2004).

Temperature-sensitive rheological modeling of crosslinked gels identified significant viscosity degradation above 160°C (Kumar et al., 2023). Hybrid discrete-continuum fracture interaction models showed enhanced stimulated reservoir volume in naturally fractured systems (Alvarez et al., 2024). Data-driven calibration techniques using diagnostic fracture injection tests (DFIT) improved estimation of formation permeability and closure pressure (Rahman et al., 2024). Stage spacing optimization studies in horizontal wells confirmed the importance of stress shadow management for maximizing cluster efficiency (Singh et al., 2025). Artificial intelligence-assisted fracture matching workflows demonstrated improved predictive accuracy compared to traditional manual calibration (Morales and Chen, 2025).

3. Methodology

3.1. Well Geometry and Completion Definition

In this study, a comprehensive set of wellbore geometric and completion parameters was defined and incorporated into the numerical model to ensure accurate representation of well behavior and stimulation conditions. The input dataset included the measured depth (MD) and true vertical depth (TVD) of all casing and liner strings, their respective setting depths, and the complete directional survey information, including inclination and azimuth along the well trajectory. These data were essential to reconstruct the three-dimensional well path and to correctly position the treatment interval within the geomechanically framework of the reservoir. Detailed specifications of both open-hole and cased-hole intervals were incorporated. The completion strategy was explicitly defined, distinguishing whether the target interval was completed as an open hole or as a cased and perforated section. In perforated completions, the exact depth and length of perforated clusters were implemented. The completion type plays a critical role in determining near-wellbore stress redistribution, fracture initiation pressure, fluid entry conditions, and early-stage fracture geometry. Therefore, precise implementation of these parameters was fundamental to achieving realistic simulation outcomes.
A schematic representation of the wellbore geometry and completion configuration is provided in Figure1. This schematic illustrates the vertical and directional well path, the setting depths of the 18 5/8-inch, 13 3/8-inch, and 9 5/8-inch casing strings, the 7-inch liner, and the 5-inch liner used to complete the Sarvak

formation. The schematic also highlights the open-hole and perforated sections, thereby clarifying the near-wellbore stress distribution and fracture initiation points used as input to the geomechanically model. As shown in Figure1, this visual representation integrates the geometric data with the completion strategy, bridging the wellbore model (e.g., built in PIPESIM) and the subsequent geomechanically analysis for optimum acid fracturing interval selection.

3.1.1 Hydraulic Modeling of a Deep Multi-String Completion Well Using PIPESIM

The schematic derived from simulation in PIPESIM software represents the hydraulic model of a deep well with multi-string completion, employed to analyze multiphase flow behavior and pressure drop along the production pathway from the reservoir to the wellhead. In this model, the total well depth is set at 3865 meters, with the main production zone located within the interval of 3651 to 3687 meters. Consequently, the effective net pay thickness is 36 meters, connected to the production stream via a 5-inch liner and an end-perforation assembly.

3.1.2 Well Architecture and Nodal Selection

The mechanical architecture of the well comprises four main casing and completion sections. At the surface level, an 18⅝-inch casing is installed to an approximate depth of 60 meters, responsible for stabilizing shallow formations and isolating surface waters. Subsequently, a 13⅜-inch casing extends to a depth of 1524 meters, typically designed to control unstable intermediate formations and withstand high operational pressures. A 9⅝-inch casing continues to 2194 meters, acting as the primary protective string in the transition zone. Following this, a 7-inch liner is installed to 3347 meters, and finally, the 5-inch production liner is positioned within the interval from 3651 to 3865 meters.

According to the schematic, a nodal point (Node) is defined at an approximate depth of 3347 meters. This location is selected because it marks the change in flow diameter from the 7-inch liner to the 5-inch production section, where local pressure drop, flow regime transition, and fluid velocity variation become particularly significant. The vertical distance between the node and the production zone is about 304 meters, which constitutes the majority of the dynamic downhole pressure drop.

3.1.3 Flow Path, Pressure Drop Components, and Production Implications

In this model, the wellhead pressure is defined as 0 barg (approximately equivalent to 1 atm absolute pressure at the surface). The indication "No Surface Equipment Found" shows that the simulation aims to evaluate the inherent production capacity of the well without considering pressure losses from chokes, flowlines, or surface separators, ensuring that all calculated pressure drop is attributed solely to in-wellbore flow. As indicated by the green flow paths, reservoir fluid enters the 5-inch liner through end-perforations and then travels to the surface through two separate routes: the tubing and the annulus. The simultaneous activation of "Tubing Flow from Cpl" and "Casing Flow from Cpl" indicates modeling of dual-path flow within the well, a configuration commonly encountered where the pressure differential between tubing and annulus is small or the completion design allows limited hydraulic communication.

Given the reduction in internal diameter from 9⅝-inch to 7-inch and then to 5-inch, flow velocity increases significantly in the production zone. Approximately, for a constant production rate, reducing the diameter from 7-inch to 5-inch more than doubles the fluid velocity, leading to higher frictional pressure drop, intensified turbulent flow, and an increased likelihood of phenomena such as liquid loading or multiphase

flow instability. In the PIPESIM hydraulic model, the total wellbore pressure drop typically consists of three main components: hydrostatic pressure drop due to the fluid column height of 3865 meters, frictional pressure drop caused by fluid contact with tubing and liner walls, and acceleration pressure drop resulting from velocity changes and multiphase flow regime transitions. In deep wells analogous to this model, the hydrostatic pressure contribution usually accounts for 60–80% of the total pressure drop, whereas frictional losses depend on production rate, wall roughness, and gas-to-liquid ratio. Furthermore, the vertical distance from the bottomhole to the surface (3865 meters) generates a significant pressure and temperature gradient along the flow path, causing thermodynamic properties of the fluid—including density, viscosity, gas compressibility, and surface tension—to vary along the wellbore. PIPESIM incorporates these changes in a coupled manner within its multiphase flow calculations to accurately replicate the real behavior of the production system. From a production engineering perspective, this model indicates that the well possesses a long, multi-section production path with substantial geometric variations; therefore, selecting the optimal tubing diameter, controlling pressure drop, and preventing flow instability will play key roles in optimizing the production rate. Results from such simulations are typically used to determine the optimal production rate, design wellhead chokes, assess the need for artificial lift, and perform sensitivity analysis of wellhead pressure versus flow rate.

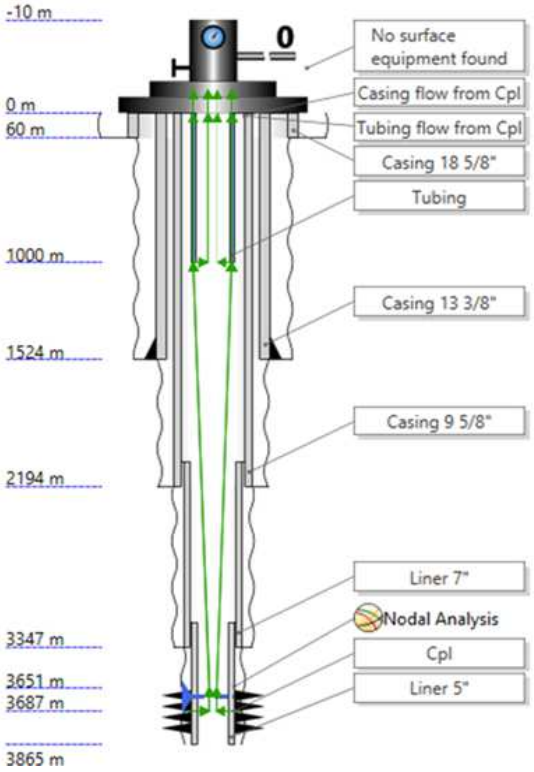


Fig. 1. One-Dimensional Wellbore Flow Model Developed in PIPESIM Software for the Depth Interval of 3120–3855 meters (Ilam and Sarvak Formations) for Well A-1

3.2. Geomechanically and Rock Mechanical Characterization

To simulate reservoir deformation and fracture propagation, key geomechanically and rock mechanical properties were defined. These included Young's modulus (YME), Poisson's ratio, additional elastic moduli where required, fracture toughness, and the fluid leak-off coefficient. Young's modulus and Poisson's ratio

were used to characterize the elastic response of the formation under induced stresses, while fracture toughness quantified the resistance of the rock to crack initiation and propagation. The leak-off coefficient was introduced to model time-dependent fluid loss from the fracture into the porous formation, which directly controls fracture width evolution and limits fracture extension. Parameter values were selected based on laboratory core testing, well log interpretation, and validated field measurements to ensure consistency with in-situ reservoir conditions. This integrated characterization provided the mechanical framework governing fracture growth and interaction with the surrounding formation.

After establishing the structural framework, a two-step geostatistical modeling approach was applied to the geomechanically data of the Bangestan reservoir, including principal stresses, Poisson's ratio, Young's modulus, pore pressure, and tectonic reservoir strains. The first step involved variogram analysis, followed by three-dimensional geomechanically modeling. Prior to this, these datasets had been analyzed within one-dimensional models covering the entire Bangestan reservoir (Ilam and Sarvak formations).

Table 2. Summary of petrophysical and geomechanical properties obtained from laboratory measurements and geomechanical zonation of well A-1.

Parameter	Symbol	Unit	Minimum	Maximum	Remarks
Bulk Density	ρ	g/cm³	2.11	2.79	Indicates lithological and compaction variations
Porosity	Φ	%	0.01	17.92	Reflects heterogeneity in pore structure
P-wave Velocity	V_P	m/s	3379	6190	Higher values indicate more compact intervals
S-wave Velocity	V_S	m/s	1725	3715	Sensitive to internal rock structure
Dynamic Young's Modulus	Edyn	GPa	16.9	79.8	Represents elastic stiffness of the rock
Poisson's Ratio	ν	–	-0.05	0.42	Describes elastic deformation behavior
Uniaxial Compressive Strength	UCS	MPa	21.78	199.55	Indicates variation in rock strength
Brazilian Tensile Strength	BTS	MPa	1.27	12.61	Tensile resistance of rock samples
Cohesion	C	MPa	2.62	58.60	Derived from triaxial testing
Internal Friction Angle	φ	Degree	8.69	63.45	Controls shear failure behavior

Laboratory measurements in table 2 indicate considerable variability in petrophysical and geomechanical properties across the studied samples. Porosity exhibits a wide distribution, suggesting heterogeneous pore structures, while UCS and elastic parameters indicate transitions from moderately strong to very strong rock intervals.

The laboratory results indicate considerable variability in the petrophysical and geomechanical characteristics of the investigated rock samples, reflecting substantial heterogeneity within the studied formation. Porosity values exhibit a broad range, varying from nearly negligible values (~0.01%) up to approximately 17.92%, suggesting the coexistence of highly compact intervals alongside more porous zones. Such variability may be associated with differences in depositional environments, diagenetic alterations, pore system evolution, and cementation intensity. Furthermore, bulk density values range from approximately 2.11 to 2.79 g/cm³, indicating variations in mineralogical composition and compaction degree. An inverse relationship between porosity and density is evident, where increased porosity generally corresponds to lower density values due to greater pore volume and reduced matrix compactness.

Ultrasonic measurements also reveal substantial variations in elastic properties. P-wave velocity varies from approximately 3379 to 6190 m/s, while dynamic Young's modulus ranges between 16.9 and 79.8 GPa. These variations suggest significant differences in rock stiffness and elastic behavior among samples. Generally, intervals characterized by higher acoustic velocities exhibit greater elastic moduli, implying more consolidated and mechanically competent rock units. Such behavior indicates that acoustic wave propagation is strongly influenced by pore structure, internal discontinuities, and overall rock fabric.

Mechanical properties derived from laboratory testing further demonstrate pronounced heterogeneity across the studied samples. Uniaxial compressive strength (UCS) values vary considerably, ranging from approximately 21.78 MPa to 199.55 MPa, indicating transitions from moderately strong to very strong rock intervals. Higher UCS values are commonly associated with increased elastic modulus values, suggesting a positive correlation between rock stiffness and compressive resistance. This trend implies that stronger rock units generally possess enhanced load-bearing capacity and greater resistance to deformation.

Similarly, indirect tensile strength values range from approximately 1.27 to 12.61 MPa and remain significantly lower than corresponding compressive strengths, which is consistent with the brittle mechanical behavior commonly observed in sedimentary formations. This discrepancy between compressive and tensile resistance highlights the susceptibility of the rock mass to tensile failure and fracture propagation under stress conditions.

In addition, multistage triaxial test results indicate notable variations in shear strength parameters. Cohesion values range from approximately 2.62 to 58.60 MPa, while friction angle values vary from 8.69° to 63.45°. Such wide distributions indicate substantial differences in failure mechanisms and shear resistance among the investigated lithological intervals. These results collectively suggest that the studied formation exhibits complex petrophysical and geomechanical behavior, where variations in pore structure and rock texture significantly influence elastic response, strength characteristics, and failure behavior.

The variations of geomechanically parameters exhibit trends similar to petrophysical properties. In the crest and northern regions of the reservoir, geomechanically parameters of the Ilam formation rocks decrease, a trend also observed in wells located at structural highs and along the flanks.

Dynamic models of Poisson's ratio and Young's modulus show the strongest correlation with porosity. Specifically, geomechanically parameters in dense, low-porosity zones are significantly higher than in high-porosity zones, indicating a clear relationship between rock mechanical behavior and reservoir petrophysical characteristics

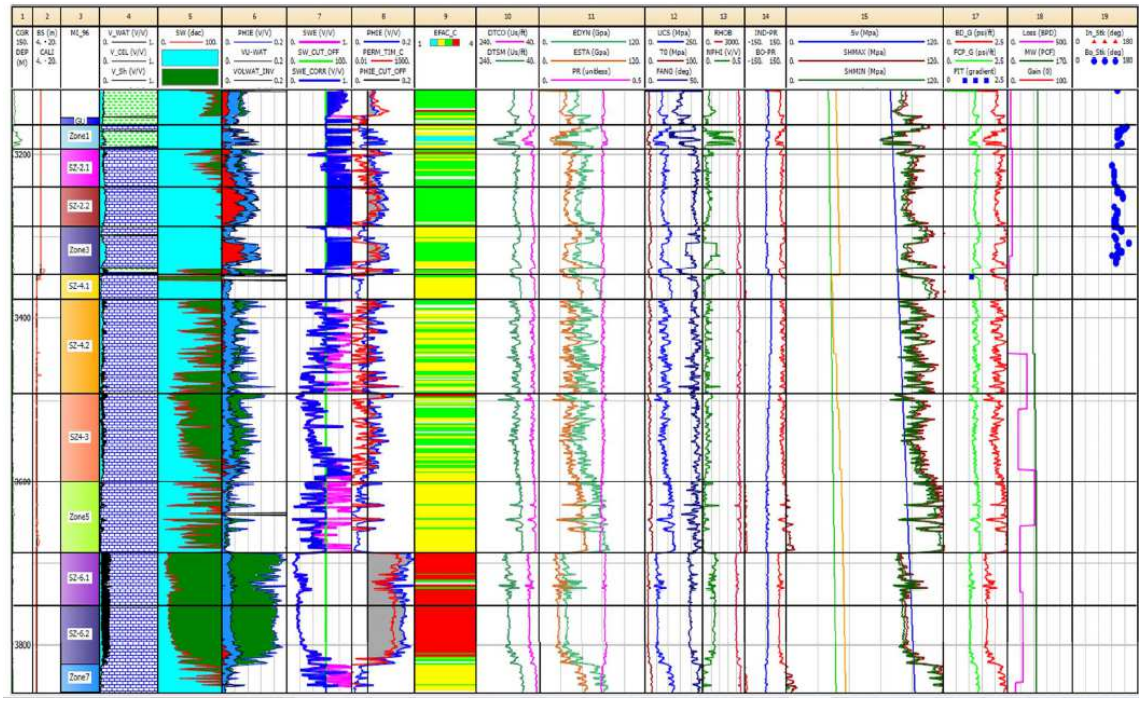


Fig. 2. Geomechanically model constructed using field-acquired data from the target well and.

Figure 2 shows that after Zone 5 (from approximately 3750 m onward), a noticeable change in fluid saturation occurs, where oil saturation exhibits an increasing trend. Concurrently, in Zones 6.1 and 6.2, a significant reduction in water saturation is observed, indicating an improvement in reservoir quality and an enhanced hydrocarbon-bearing capacity within these intervals.

From a petrophysical and geomechanical perspective, these zones are characterized by increased permeability and are classified as Rank 4 according to the EFAC-C classification, representing moderate to good reservoir quality. In addition, both static and dynamic elastic moduli of the rock decrease to values below 30 GPa, reflecting reduced rock stiffness and increased mechanical compliance of the formation.

In terms of in-situ stress distribution, the maximum and minimum horizontal stresses are lower than the vertical stress within this interval, indicating a transition in the stress regime that influences the mechanical behavior of the formation. Consequently, both breakout and fracture initiation pressure gradients (FCP) show a decreasing trend, suggesting improved borehole stability and a reduced tendency toward mechanical instability in these zones.

From a drilling performance standpoint, mud losses in this interval are estimated at approximately 5 barrels per hour, which is considered acceptable and indicative of good hydraulic connectivity with the formation. Given a drilling mud weight of approximately 65 pcf, these conditions suggest a relatively balanced pressure regime between formation pressure and hydrostatic mud pressure, reflecting controlled and stable drilling conditions.

Zones 4.1, 4.2, and 4.3, despite exhibiting the presence of oil saturation, are characterized by relatively high-water saturation and comparatively low porosity (generally below 3%) when compared to Zones 6.1 and 6.2. These petrophysical conditions indicate that the reservoir quality in these intervals is not favorable in terms of EFAC-C classification, as they predominantly fall within Rank 2 and only sporadically achieve Rank 3 in limited localized sections.

As a result of these characteristics, the mechanical behavior of the rock reflects a more competent and rigid formation. Both static and dynamic elastic moduli are relatively high, indicating increased rock stiffness. In addition, the unconfined compressive strength (UCS), tensile strength (T_0), and internal friction angle (FANG) all exhibit elevated values, consistent with a mechanically stronger and more brittle rock fabric.

A key consideration in acid fracturing modeling is that, based on the achieved fracture penetration radius and the estimated volume required to obtain useful conductivity, the fracture height should not enter the upper and lower adjacent zones. The upper layer corresponds to Zone 5 with its specific characteristics. The lower layer corresponds to the saline water zone within the aquifer, i.e., Zone 7 and deeper. This constraint is incorporated into the subsequent simulation to ensure that the fracture radius does not extend into the water-bearing layers above and below the target interval.

Referring to the geomechanical model image (Figure 2), it illustrates the vertical distribution of key reservoir properties and mechanical parameters along the wellbore trajectory in Well A-1. The figure shows that below Zone 5 (approximately from 3750 m onward), oil saturation exhibits an increasing trend, while water saturation decreases significantly in Zones 6.1 and 6.2, indicating improved reservoir quality and enhanced hydrocarbon-bearing capacity. Furthermore, the static and dynamic elastic moduli decrease to values below 30 GPa in these zones, reflecting reduced rock stiffness and increased mechanical compliance. Regarding in-situ stress distribution, the maximum and minimum horizontal stresses are lower than the vertical stress within this interval, indicating a transition in the stress regime that influences the mechanical behavior of the formation. Consequently, both borehole breakout and fracture initiation pressure gradients show a decreasing trend, suggesting improved borehole stability and reduced tendency toward mechanical instability. In contrast, Zones 4.1, 4.2, and 4.3, despite the presence of oil saturation, exhibit relatively high water saturation and low porosity (generally below 3%), indicating poor reservoir quality. In these zones, elastic moduli, unconfined compressive strength, tensile strength, and internal friction angle all show elevated values, consistent with a mechanically stronger and more brittle rock fabric.

3.3. Fracturing Fluid Properties and Flow Modeling

Accurate simulation of the hydraulic fracturing process required detailed characterization of the fracturing fluid. Friction pressure loss tables for flow within tubulars and inside the fracture were incorporated as functions of injection rate and fluid properties, allowing precise computation of pressure gradients and stress distribution along the flow path. The rheological behavior of the fluid was defined based on its non-Newtonian characteristics. Rheological parameters were tabulated under relevant shear rate and temperature conditions. The fluid behavior was primarily represented using the Power-law model, with the flow behavior index (n) and consistency index (K) determined for operational conditions. This formulation enabled realistic simulation of viscosity variations under dynamic injection scenarios. Thermal effects were also considered by incorporating the specific heat capacity of the fluid to model heat exchange between the injected fluid and the formation. Temperature variations can significantly influence viscosity, reaction kinetics in reactive systems, and consequently fracture geometry. Fluid loss mechanisms were fully implemented, including the time-dependent leak-off coefficient to describe filtration into the porous matrix and the spurt loss term to represent rapid initial fluid invasion upon fracture opening. Incorporating both mechanisms allowed accurate prediction of effective fracture fluid volume and geometric development over time.

Table 1. Input Parameters for Acid Fracturing Simulation in Well A-1 (Zone 6.1 and 6.2)

Parameter	Value	Unit
Wormhole breakthrough pore volume (Q_{ibt})[1]	1.5	-
Formation Rock Density (ρ_{Rock})	2600	kg/m^3
Reservoir Oil Viscosity (μ_{Oil})	1.66	cp
Reservoir Temperature (T)	248	°F
Reservoir Depth	3910	Ft
Fracturing Pressure (p_f)	6300	Psi
Reservoir Pressure (p_r)	5121	Psi
Gas Specific Gravity	1.227	-
Oil Specific Gravity	24.3	-
Water Specific Gravity	1.19	-
Gas Saturation	0	Frac
Oil Saturation	0.64	Frac
Water Saturation	0.36	Frac
Total compressibility (C_t)	6.14E-05	Psi^{-1}
Oil Compressibility (C_o)	9.21E-06	Psi^{-1}
Water Compressibility (C_w)	3.2E-6	Psi^{-1}
Gas Compressibility (C_g)	6.5E-5	Psi^{-1}
Rock Compressibility (C_f)	1.05E-5	Psi^{-1}
Young's Modulus (E)	6	MMPsi
Layer Thickness (H)	102	m
Closure Stress (σ_c)	7910	Psi
Poisson Ratio (υ)	0.25	-
Permeability (k)	0.45	md
Porosity (∅)	0.087	-
Spurt loss (S_p)	0	m

Depth-specific dynamic elastic properties are computed from the following equations. These moduli are obtained from the combination of bulk density logs and acoustic transit time data for both P- and S-waves.

$$\nu_d = \frac{(V_P^2 - 2V_S^2)}{2(V_P^2 - V_S^2)} \quad \text{Equation-1}$$

$$E_d = \left(\frac{\rho\upsilon_S^2(3V_P^2 - 4V_S^2)}{V_P^2 - V_S^2}\right) \quad \text{Equation-2}$$

The primary rock strength parameters considered in this study are unconfined compressive strength (UCS), tensile strength (T_0), and internal friction angle (φ). To generate a continuous UCS log, an empirical correlation was developed from laboratory measurements by plotting UCS values against porosity or static Young's modulus. Equation 9 presents this relationship, which was further implemented in the constructed geomechanical models.

$$UCS = 2.27E_S + 4.74 \quad \text{Equation-3}$$

[1] *Q_ibt is the number of pore volumes of acid injected required for wormhole breakthrough.*

Estimation of the internal friction angle (φ) is performed using the empirical correlation proposed by Plumb (1994), which has been subsequently employed by Fjaer et al. (2008). This relationship incorporates neutron porosity (NPHI) and shale volume content as input parameters.

$$\phi = 26.5 - 37.4(1 - \mathrm{NPHI} - \mathrm{V_{Shale}}) + 62.1(1 - \mathrm{NPHI} - \mathrm{V_{Shale}})^2 \quad \text{Equation-4}$$

3.4. Pumping Schedule and Operational Constraints

The pumping schedule was defined as a dynamic boundary condition governing fracture evolution. The schedule included precise timing of treatment stages, injection rate profiles, total injected volumes, fluid sequencing (pad stage, proppant-laden slurry stages, and final flush), and time-dependent variations in proppant concentration. The temporal evolution of injection rate and proppant concentration was implemented in either stepwise or continuous form to replicate field conditions accurately. The initial pad volume was defined to ensure fracture initiation and early extension prior to proppant introduction. The proppant ramp-up schedule was explicitly incorporated to control proppant transport and placement efficiency. A final displacement or flush volume was included to clear the wellbore of residual proppant. Operational constraints, such as maximum allowable surface pressure and pump capacity limitations, were also applied where relevant. Because fracture growth is highly sensitive to injection history, accurate implementation of the pumping schedule was essential for predicting pressure evolution, final fracture geometry, and proppant distribution.

3.5. Numerical Implementation and Time-Stepping Procedure

After complete definition of well geometry, reservoir properties, fluid characteristics, and pumping schedule, the acid fracturing treatment was designed and simulated using the GOHFER software platform. In the present treatment design, proppant was intentionally not included, as the objective was to evaluate an acid fracturing strategy intended for periodic re-stimulation and repeated treatment cycles over the well life rather than relying on permanent proppant-supported conductivity. Therefore, fracture conductivity enhancement was primarily achieved through acid etching mechanisms and sustained fracture surface roughness.

The numerical model was executed using an adaptive time-stepping scheme. Time-step selection was governed by numerical stability requirements and by the need to accurately capture rapid transient behavior during fracture initiation and early-stage propagation. Smaller time steps were employed during periods of rapid pressure and fracture aperture changes, whereas larger time steps were used during relatively stable propagation stages.

At each time increment, the governing equations, including mass conservation, momentum balance, fluid flow within the fracture and formation, and geomechanically constitutive relationships, were solved in a fully coupled manner. Fracture pressure, aperture distribution, fracture length and height evolution, fluid leak-off, and effective stress changes were updated sequentially throughout the simulation process.

The simulation continued until completion of the pumping schedule and, where necessary, through the fracture closure stage. Final outputs included fracture geometry, pressure responses, and other key performance indicators used for subsequent technical analysis and treatment performance evaluation.

The figure 3(A) illustrates the relationship between injection volume/rate (q) and fracture width (W). The results indicate that fracture width initially increases with increasing injection volume, which can be

attributed to the rise in fluid pressure, improved fracture propagation, and enhanced fracture opening. As the injection volume continues to increase, the rate of width growth gradually decreases, and the fracture width reaches its maximum value of approximately 0.17 in within the range of about 22–30 bbl. Beyond this range, the fracture width enters a nearly stable region and even shows a slight decline. This behavior may be associated with increased fluid leak-off into the formation, stress redistribution around the fracture, and changes in fracture propagation mechanisms. Overall, the results demonstrate a non-linear relationship between injection volume and fracture width, indicating the existence of an optimum injection range for achieving maximum fracture opening.

3.5.1 Selection of Optimum Injection Rate

To determine the optimum fluid injection rate, the total injected fluid volume during the treatment was assumed constant, while the effects of injection rate on fracture length, fracture height, and fracture width were investigated. The obtained results are presented in Figures 3.1 to 3.3.

According to Figure 3.1, increasing the fluid injection rate results in an increase in the generated fracture width. This increasing trend continues up to a specific point highlighted in red, after which the fracture width approaches a nearly constant behavior. The identified point corresponds to an injection rate of approximately **22 bbl/min**, indicating a threshold beyond which further increases in injection rate provide negligible improvements in fracture aperture.

According to Figure 3.2, fracture length initially increases with increasing fluid injection rate. However, this trend exhibits a periodic or oscillatory behavior at higher injection rates. Such fluctuations indicate that within each cycle, a maximum achievable fracture length exists, occurring approximately at the peak of the oscillation. The optimum condition corresponding to the maximum fracture extension was identified at an injection rate of approximately **17 bbl/min**.

As shown in Figure 3.3, increasing the injection rate leads to a gradual increase in fracture height until reaching a relatively stable region. Beyond the point highlighted in red, a sudden increase in fracture height is observed. This abrupt increase can be explained by the simultaneous reduction in fracture length shown previously in Figure 3.3, indicating redistribution of fracture growth.

3.5.2 Selection of Optimum Injected Fluid Volume

To determine the optimum injected fluid volume, the injection rate was assumed constant, and the influence of injected volume on fracture dimensions was analyzed. The corresponding results are shown in Figures 3.4 to 3.6.

According to Figure 3.4, increasing the injected fluid volume results in an increase in fracture width. This trend continues until reaching a critical point highlighted in red, beyond which the fracture width remains nearly constant. This point corresponds to an injected fluid volume of approximately 90,000 gal.

According to Figure 3.5, fracture length increases with increasing injected fluid volume and reaches a maximum value at the point highlighted in red. Beyond this point, fracture length decreases and subsequently returns to its maximum value. The optimum injected volume corresponding to this behavior is approximately 81,000 gal.

It should be noted that the sudden reduction in fracture length with increasing injected volume can be explained based on the principle of mass conservation. Assuming a constant injected fluid volume, any reduction in fracture length is compensated by an increase in fracture height generated during the treatment process. This behavior is illustrated in Figure 3.6.

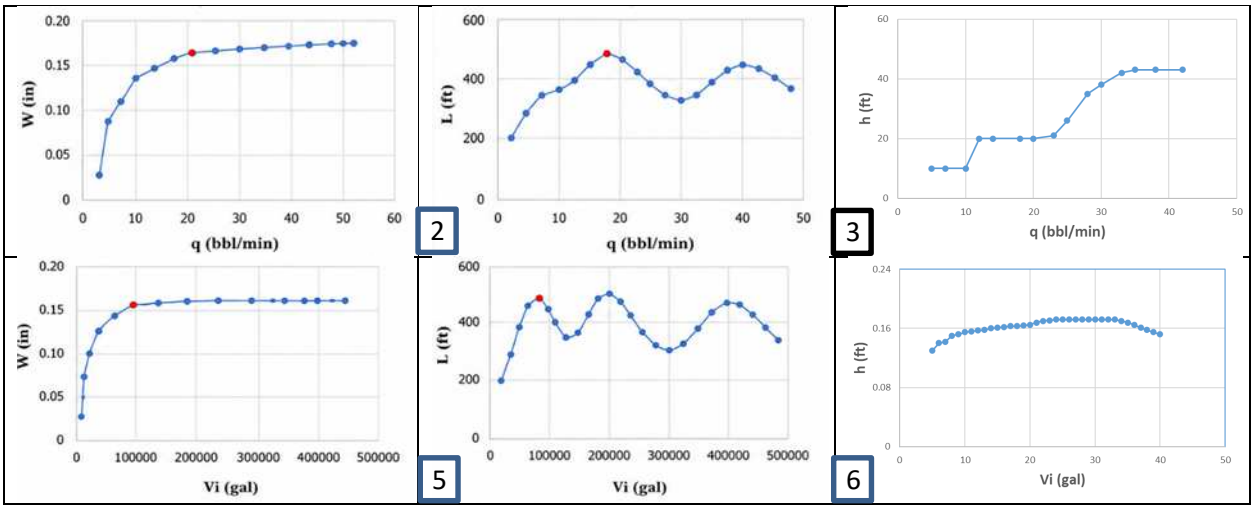


Fig. 3. Sensitivity analysis of fracture geometry parameters with respect to operational injection conditions. Figures (3.1–3.3) illustrate the effect of injected flow rate (q, bbl/min) on fracture dimensions, including fracture width (W), fracture length (L), and fracture height (h), respectively. Figures (3.4–3.6) present the influence of injected fluid volume (Vi, gal) on fracture width, fracture length, and fracture height, respectively. The results demonstrate the variation of fracture geometry under different operational conditions and provide insight into identifying optimum treatment parameters for acid fracturing design.

5. Acid Fracture model

Figure 3 presents the variations in simulation parameters during the hydraulic fracturing process in the Bangestan Formation. The model includes key parameters such as fracture size, fracture width, pump rates, pump pressure, and efficiency. The start and end times of all four graphs are identical. Figure 3-a illustrates the changes in fracture length over a period of 55 minutes. The fracture length increased gradually until minute 32; however, after this point, the changes became negligible. Figure 3-c depicts the variation in fracture width over a 55-minute period. Initially, the fracture width measured 0.02 inches, doubling within approximately 8 minutes. After 36 minutes, it gradually increased from 0.04 inches to 0.1 inches, likely due to the volumetric expansion of the rock along the axis of the applied force. Figure 3-b illustrates the variations in rock fracture pressure throughout the duration of applied pressure, ultimately reaching a maximum of 10,800 psi. It is evident that this value of 10,800 psi corresponds solely to rock fracturing based on its petrophysical properties. However, in the case of perforated well completions, an additional pressure drop of 5,000 to 6,000 psi must be considered. Figure 3-d illustrates the increase in fracture height over the duration of applied pressure. The fracture height exhibited two distinct growth trends. During the first 15 minutes, it expanded at a higher rate compared to the final 40 minutes. A planar 3D fracture model was developed using GOHFER, a fully coupled 3D fracture simulator. It designed to simulate the transfer of rock and fluid through a repetitive grid representing hydraulic fracture development.

The software accounts for reservoir characteristics, changes in rock properties, and stresses in order to simulate crack growth and evaluate production conditions after failure. Based on the minimum horizontal stress and applied tectonic stress, the software estimated the fracture pressure within the formation. These values were calculated for the well A-1 in the Bangestan Reservoir, located in the field, at a depth of 3540 meters.

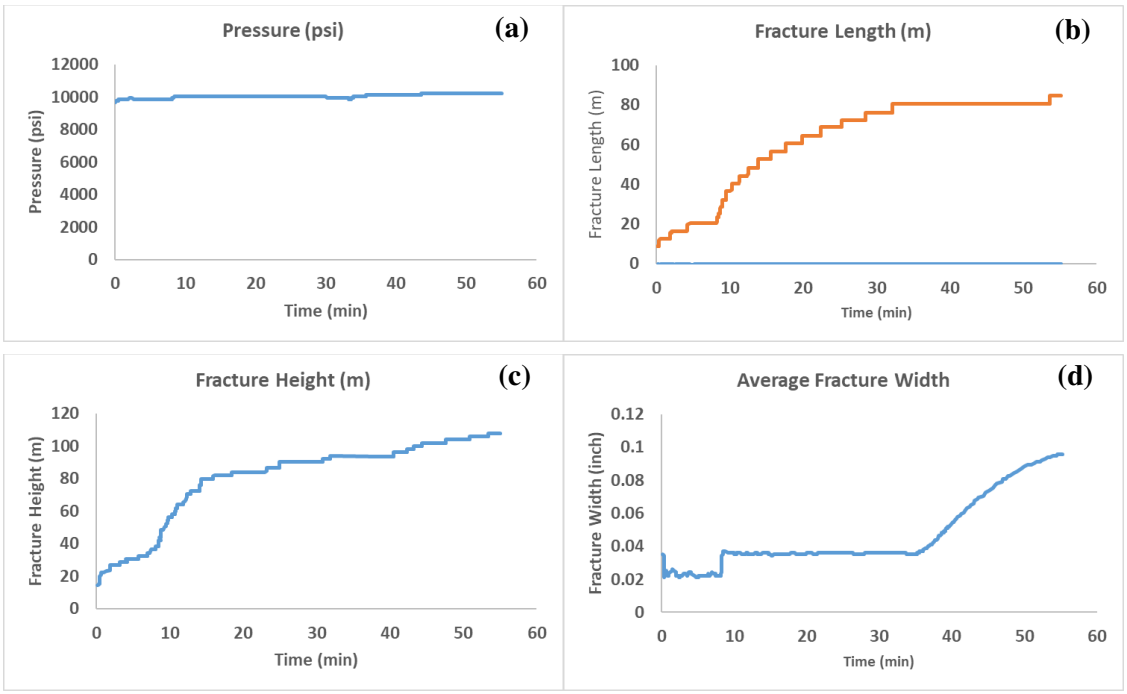


Fig. 3. Results of fracture geometry simulation in a carbonate reservoir formation (including real petrophysical rock conditions) using GOHFER software; a) Pressure(psi) vs. Time b) Fracture Length(m) vs. Time, c) Fracture Height(m) vs. Time(min), d) Fracture width(inch) vs. Time (min)

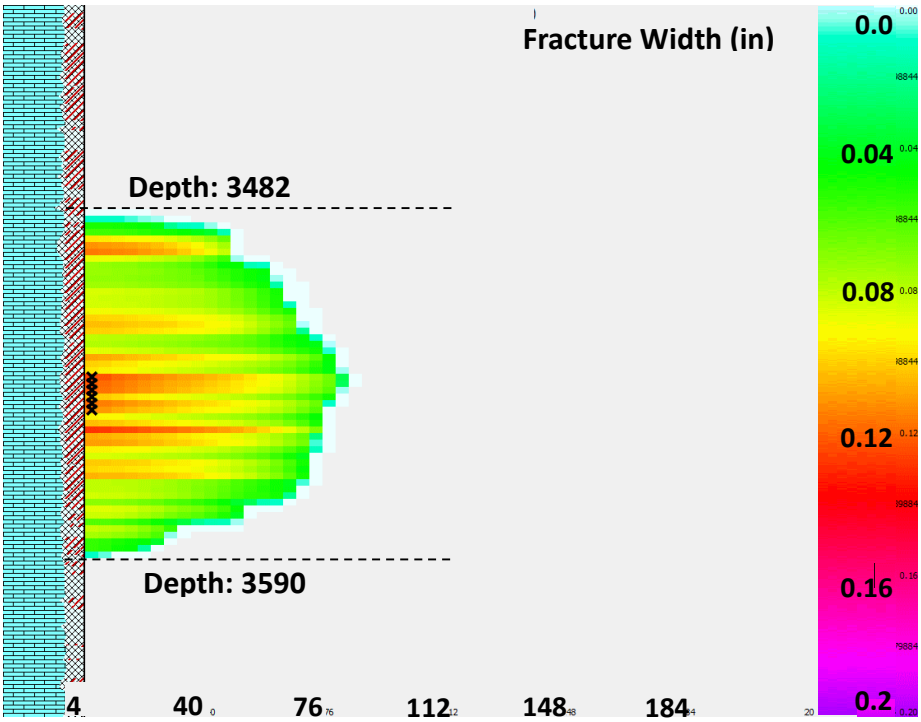


Fig. 4. The width of the fracture created with the Gohfer software at the end of the pad stage

Figure 4 also depicts variations in the fracture width on the fracture plane in the fracture geometry model, where the red points indicate wider widths. The Figure 5-a illustrates changes in pressure on the fracture plane in the fracture geometry modeling. The pressure required to induce the fractures has been simulated.

Figure 5-b illustrates the pressure distribution on the fracture plane, and numerical values corresponding to it have been identified based on the color variation guide in the image.

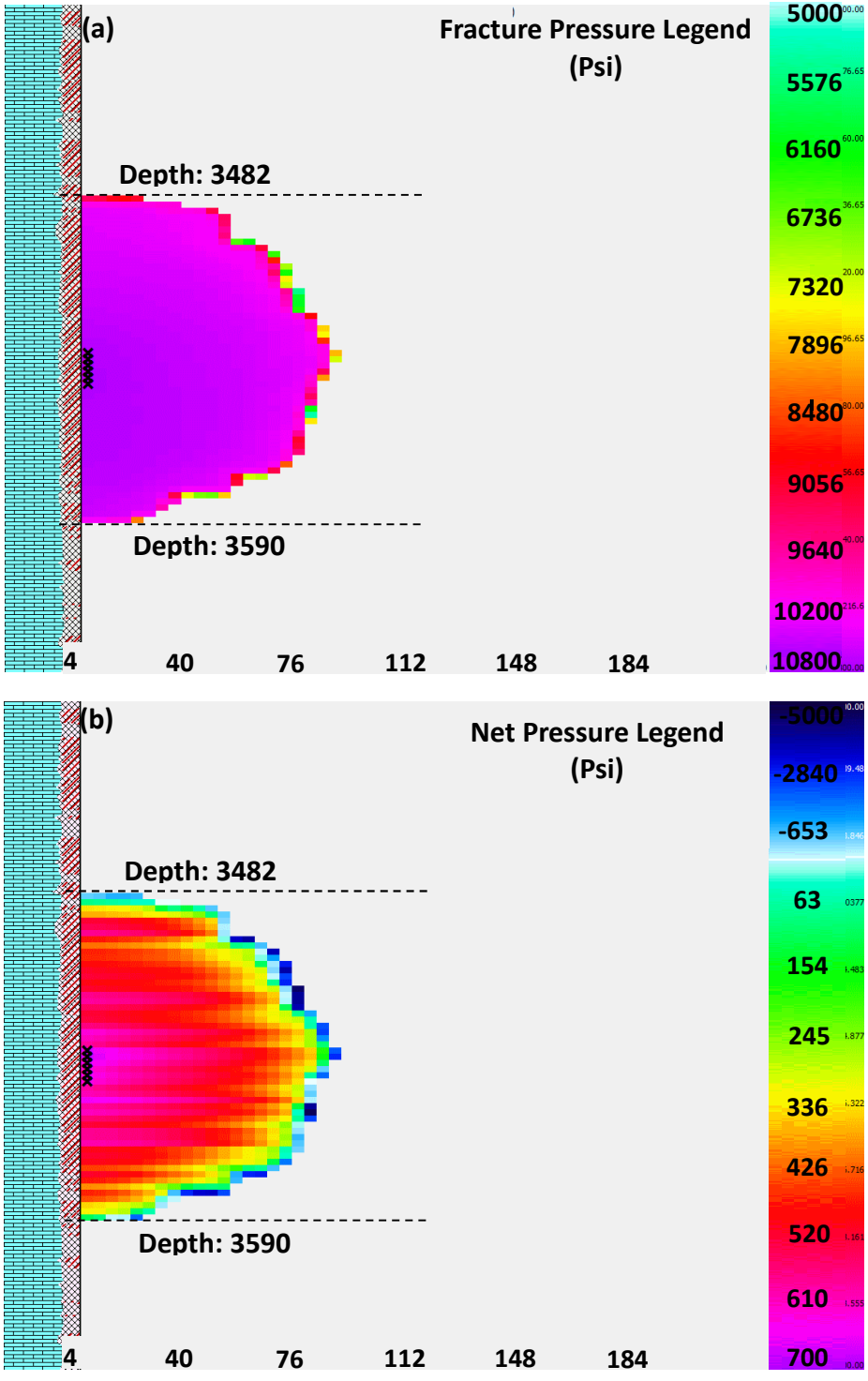


Fig. 5. Pressure parameters measured with Gohfer software. a) failure development pressure b) net pressure

6. Operational Validation of Geomechanical Model Using Field Data

The XLOT/FBP test response represents the complete hydro-mechanical behavior of the formation under progressive fluid injection and subsequent shut-in conditions, and it can be interpreted as a continuous sequence of elastic response, fracture initiation, propagation, and closure processes. At the beginning of the test, the pumping pressure increases linearly, indicating that the formation is still in the elastic regime where deformation is fully reversible and no significant damage has yet occurred. This stage corresponds to the Formation Integrity Test (FIT), during which the pressure rises up to approximately 2,800 psi, representing the initial capacity of the formation to withstand fluid invasion without failure.

With further increase in pressure, the curve deviates from linearity and reaches the Leak-Off Pressure (LOP) at approximately 5,920 psi. At this point, the first microfractures are activated and fluid begins to leak into the formation, indicating the onset of non-linear and damage-controlled behavior. This marks the transition from intact elastic response to progressive microcrack development within the rock matrix.

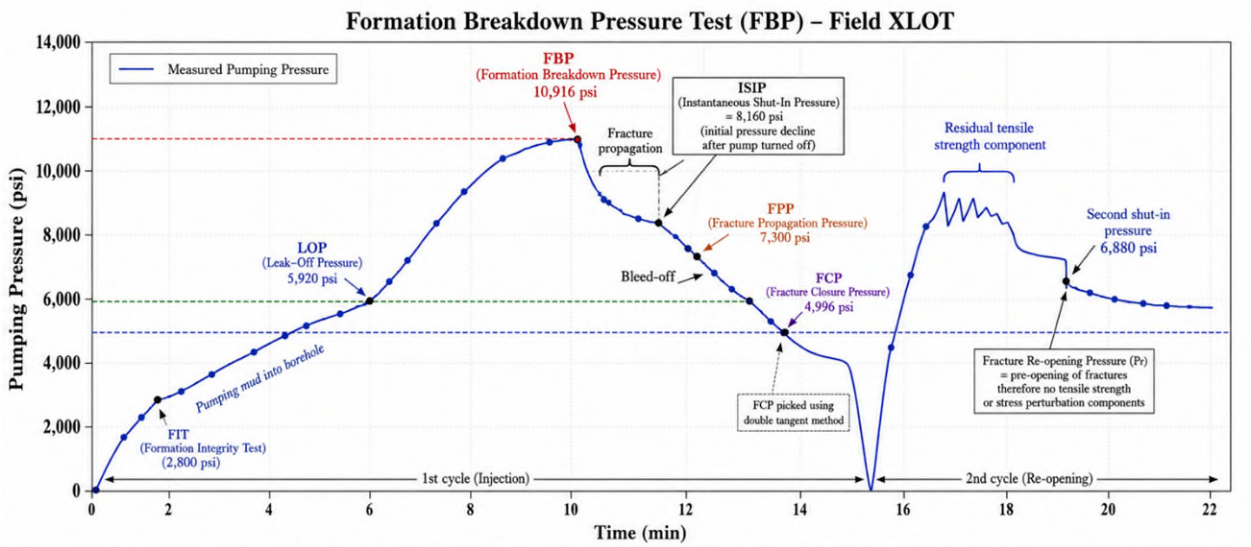
As the pressure continues to increase, the system reaches the peak of the curve, corresponding to the Formation Breakdown Pressure (FBP) at approximately 10,916 psi. This is the critical point at which the effective tensile stress exceeds the rock strength, leading to the initiation of a stable hydraulic fracture and the creation of a dominant flow pathway. From a geomechanical perspective, this pressure reflects the combined effect of in-situ stresses, pore pressure, and tensile strength of the rock.

Immediately after pumping is stopped, the pressure drops rapidly to the Instantaneous Shut-In Pressure (ISIP), which is approximately 8,160 psi. This value is considered a reliable proxy for the minimum horizontal stress (Shmin) and represents the equilibrium pressure of the newly created fracture once fluid injection ceases. It reflects the balance between fracture opening pressure and in-situ stress field.

As the pressure further declines, the Fracture Propagation Pressure (FPP) is observed at around 7,300 psi, which represents the pressure required to sustain and continue fracture growth against the resistance of the surrounding rock and viscous fluid losses. With continued pressure decline, the fracture begins to close, and the Fracture Closure Pressure (FCP) is identified at approximately 4,996 psi. This point is of major geomechanical importance, as it is commonly used as a direct indicator of the minimum horizontal stress (Shmin), representing the stress at which the fracture surfaces come into contact.

During the bleed-off phase, the pressure decline continues due to fluid leak-off from the fracture network and gradual reduction in fracture conductivity. In the second cycle of the test, fracture re-opening behavior is observed, where the Re-opening Pressure (Pr) is significantly lower than the initial breakdown pressure, occurring at approximately 6,880 psi. This reduction indicates that the pre-existing fracture requires less energy to be reactivated due to damage and weakening of the fracture surfaces.

Finally, fluctuations observed in the residual pressure stage reflect the residual tensile strength component and the heterogeneity of the fracture surfaces, indicating frictional sliding and partial closure effects within the fracture network. Overall, the results clearly indicate a brittle formation behavior with well-defined fracture initiation and closure stages, and a significant difference between FBP, ISIP, and FCP, which provides reliable constraints for in-situ stress estimation and fracture mechanics interpretation.



Test Summary	
Total Test Time	20 min
Total Mud Injected	2.8 bbl
Average Pump Rate	0.5 bpm
Mud Density	77 pcf
Mud Type	B.O
Test Type	Leak-Off & Extended Leak-Off

Depth Information	
Test Interval	3369–3374 m MD
Interval Thickness	4.0 m
RTTS Depth	3335 m MD
Casing Shoe Depth	3369 m MD

Key Pressure Results (1st Cycle)	
FIT (Formation Integrity Test)	2,800 psi
LOP (Leak-Off Pressure)	5,920 psi
FBP (Formation Breakdown Pressure)	10,916 psi
ISIP (Instantaneous Shut-In Pressure)	8,160 psi
FPP (Fracture Propagation Pressure)	7,300 psi
FCP (Fracture Closure Pressure)	4,996 psi

2nd Cycle Results	
Fracture Re-opening Pressure (Pr)	6,880 psi
Residual Tensile Strength Component	≈ 8,900 psi (peak)
Second Shut-In Pressure	6,980 psi

Test Conditions	
Pumping Equipment	Cement Pump
Pressure Rating	15,000 psi
Max Surface Pressure	4,996 psi
Equivalent Mud Column	5,920 psi

Note: Pressures are reported at surface conditions.

7. Discussion

The integrated geomechanically acid fracture simulation performed in this study demonstrates the strong interdependency between in-situ stress conditions, rock mechanical properties, fluid-loss mechanisms, and fracture geometry evolution in carbonate formations. The calibrated model, implemented using GOHFER, enabled realistic prediction of fracture propagation behavior under field-representative operational constraints.

7.1. Influence of In-Situ Stress and Stress Regime

The stress regime identified in the Ilam and Sarvak formations indicates a predominantly normal faulting system (Sv > SH > Sh). Under this regime, fracture growth is primarily controlled by the minimum horizontal stress (Sh), which governs fracture opening and lateral propagation. Sensitivity analyses showed that relatively small variations in Sh significantly altered fracture containment and vertical growth behavior. An increase in Sh reduced fracture height growth and promoted lateral extension, while a decrease allowed greater vertical propagation into adjacent layers. This behavior confirms that accurate stress calibration—especially through breakout and stability analysis—is essential for reliable fracture design. In layered carbonate systems such as Bangestan, even moderate stress contrasts between sublayers can act as effective vertical barriers or, conversely, allow height growth if stress differences are small.

7.2. Role of Elastic Properties and Fracture Toughness

Young's modulus (6 MMpsi) and Poisson's ratio (0.25), listed in Table 1, were key mechanical parameters directly affecting fracture width development and net pressure response. Higher stiffness resulted in narrower fractures and increased net pressure, whereas lower stiffness promoted wider apertures for the same injection conditions. Because etched fracture conductivity in acid fracturing strongly depends on

effective fracture width prior to closure, uncertainties in elastic parameters translate directly into uncertainties in post-treatment productivity. This highlights the importance of static-dynamic modulus conversion and core-based calibration in carbonate formations.

7.3. Leak-Off and Acid Efficiency

The leak-off coefficient and the fraction of acid reacting before leak-off (f_r = 0.3) played a dominant role in controlling fracture extension and effective acid penetration. Unlike propped fracturing, where fracture geometry is the primary performance metric, acid fracturing efficiency depends on the spatial distribution of acid-rock reaction along the fracture faces. High leak-off reduced effective fracture half-length by limiting fluid availability for continued propagation, but it also enhanced acid penetration into the formation matrix. Therefore, an optimal balance must be achieved between fracture extension and acid reactivity. The simulation results suggest that in low-permeability carbonate layers (k = 0.4 md), leak-off is moderate, allowing sufficient fracture growth while maintaining acid-rock interaction. However, in more permeable intervals, premature acid loss could reduce etched width development.

7.4. Pressure Evolution and Near-Wellbore Effects

The simulated breakdown pressure (~10,800 psi) reflects formation mechanical resistance. In perforated completions, an additional 5,000–6,000 psi pressure drop is expected due to perforation friction and near-wellbore tortuosity. This highlights the importance of accurate well completion modeling. Pressure distribution maps indicate non-uniform net pressure along the fracture plane, which directly influences local aperture variations. These spatial differences explain the heterogeneous fracture width patterns observed in Figure 4. Such heterogeneity is critical in acid fracturing because local variations in aperture strongly affect acid transport, diffusion, and dissolution kinetics. By increasing the fracture width parameter from 0.00833 ft to 0.025 ft, the production rate increased by approximately 80 barrels per day, while the bottomhole flowing pressure decreased by about 15 psi.

Figure above illustrates the nodal analysis results obtained from PIPESIM for Well_1 under different tubing internal diameter scenarios. The analysis was conducted to evaluate the interaction between reservoir inflow performance and vertical lift performance (VLP) and to determine the optimum operating point for the production system. In this plot, the vertical axis represents the pressure at the nodal analysis point in psia, while the horizontal axis represents the stock-tank liquid production rate in STB/d. The nearly horizontal light-blue curve corresponds to the reservoir inflow performance relationship (IPR), whereas the descending-colored curves represent the outflow or VLP performance for different tubing inside diameters (WIDTH). The inflow curve remains relatively stable around 3850–3900 psia across a broad production range, indicating that the reservoir possesses relatively strong pressure support and moderate productivity decline with increasing production rate. This behavior suggests that reservoir deliverability is not the primary limiting factor in the production system; instead, the dominant constraint arises from wellbore hydraulic losses. Five different tubing internal diameters (2.5, 3, 4, 5, and 6 inch) were analyzed in the simulation.

The corresponding vertical lift performance (VLP) curves reveal a clear hydraulic trend. As tubing diameter increases, frictional pressure losses decrease significantly, shifting the outflow performance curves toward higher production rates. Conversely, smaller tubing diameters generate steeper pressure gradients due to increased fluid velocity and wall shear stress, thereby limiting the achievable flow rates.

The intersection points between the inflow performance relationship (IPR) and VLP curves define the stable operating conditions of the well. Based on the simulation results, the operating point for the smallest tubing diameter (2.54 in) occurs at a production rate of approximately 600–650 STB/d and a nodal pressure of about 3900 psia. For the 3-in tubing configuration, the operating rate increases to approximately 700–750 STB/d at a nodal pressure of approximately 3880 psia. For the 4-in tubing scenario, the operating point shifts further to 800–850 STB/d at about 3860 psia. The 5-in tubing design yields a production rate of approximately 900–950 STB/d at a nodal pressure of nearly 3850 psia. Finally, the largest tubing diameter (6 in) provides the highest deliverability, with an operating rate approaching 1000–1050 STB/d at a nodal pressure of about 3840 psia.

These results indicate that increasing the tubing diameter from approximately 2.5 in to 6 in improves liquid production capacity by nearly 60–70%. This enhancement is primarily attributed to the reduction in frictional pressure losses along the 3865 m vertical flow path.

The curvature of the VLP curves also provides important hydraulic insight. At low production rates, the pressure drop is dominated by hydrostatic effects, resulting in relatively linear behavior. However, at higher flow rates, frictional losses increase nonlinearly due to turbulence and multiphase flow interactions. Consequently, the VLP curves exhibit progressively steeper declines at higher production rates, especially for smaller tubing diameters.

The analysis further demonstrates that smaller tubing sizes reach critical hydraulic conditions earlier than larger diameters. For instance, the 2.54-in tubing curve collapses rapidly beyond approximately 2000 STB/d, indicating severe frictional losses and the possible onset of unstable multiphase flow behavior, such as slug flow or liquid loading. In contrast, the 6-in tubing maintains lower pressure losses over a broader production range and sustains flow rates close to 2400 STB/d before approaching near-zero bottomhole pressure conditions.

The sensitivity analysis presented in the lower-left figure evaluates the effect of fracture permeability on the production rate. The results indicate that increasing fracture permeability from approximately 10,000 md to 50,000 md raises the production rate from nearly 450 STB/d to approximately 900 STB/d. However, the production increase becomes progressively smaller at higher permeability values, indicating diminishing returns due to hydraulic limitations in the wellbore system rather than reservoir inflow restrictions.

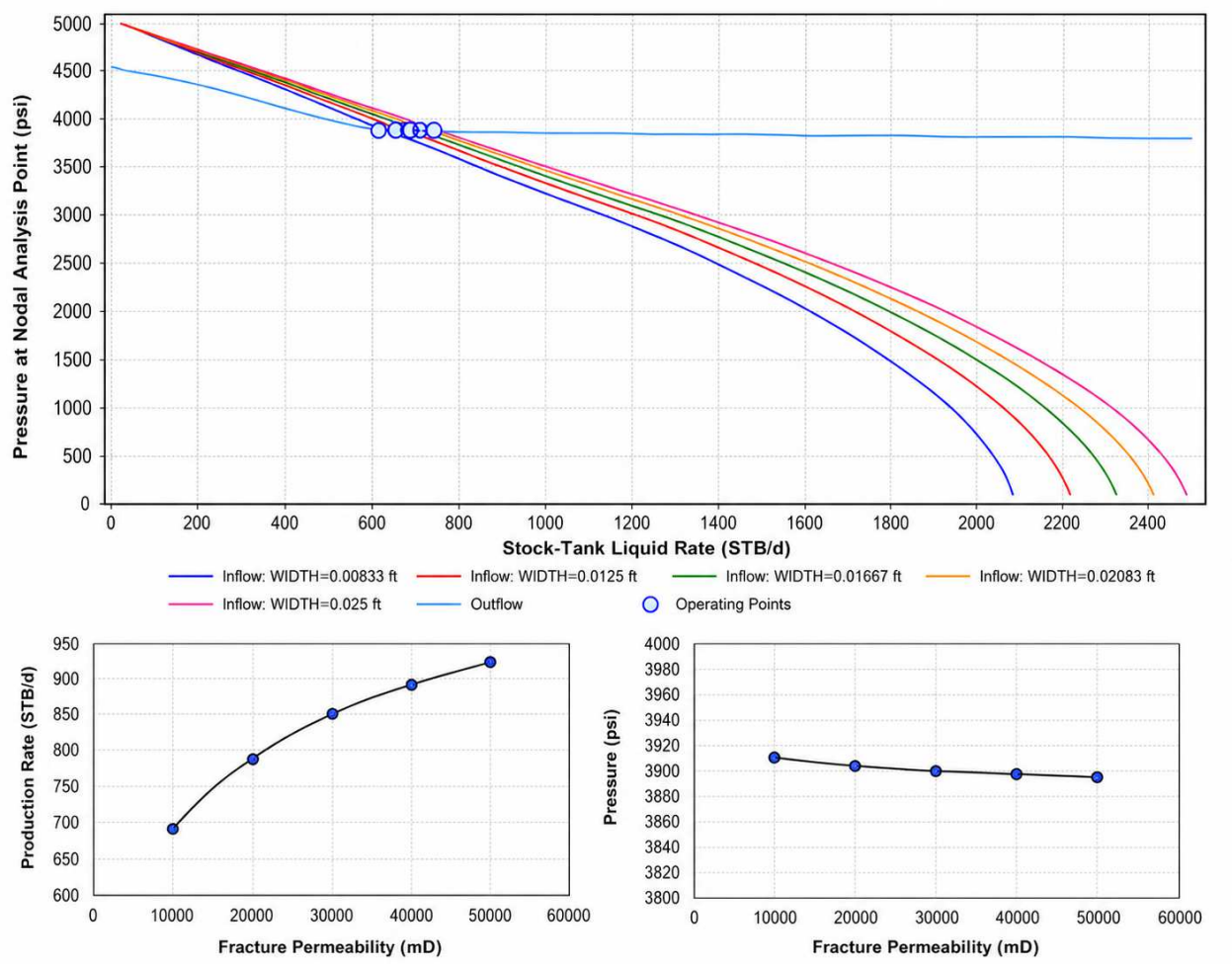


Fig. 6. A) Sensitivity Analysis Results on Fracture Permeability, B) Effect of Increasing Fracture Permeability on Well Production Rate, C) Variation of Bottomhole Pressure with Increasing Fracture Permeability

Similarly, the lower-right figure analyzes the influence of fracture permeability on the flowing pressure. As fracture permeability increases, the pressure at the nodal point decreases slightly from approximately 3920 psia to nearly 3890 psia. This relatively small pressure variation confirms that the reservoir maintains strong energy support and that wellbore hydraulics remain the dominant factor controlling production performance.

7.5. Fracture Geometry Evolution

The fracture length increased steadily until approximately 32 minutes, after which growth stabilized despite continued pumping. This plateau behavior suggests a transition toward leak-off-dominated conditions and stress equilibrium.

Fracture height exhibited two distinct growth regimes:

- Rapid early vertical expansion (first 15 minutes)
- Reduced growth rate during later stages

This indicates that early-time propagation is controlled primarily by injection rate and stress contrast, whereas later growth becomes constrained by mechanical layering and pressure redistribution.

Fracture width evolved gradually, ultimately reaching approximately 0.1 inches (0.0083 feet). In carbonate acid fracturing, this width magnitude is critical because etched conductivity is directly proportional to initial fracture aperture and subsequent surface roughness after dissolution.

7.6. Geomechanically–Hydraulic Coupling

The fully coupled modeling framework proved essential for capturing stress redistribution around the fracture. As the fracture propagates, local stresses are altered, affecting subsequent growth direction and containment. Simplified uncoupled models would not adequately reproduce these dynamic interactions. The integration of well geometry, calibrated stress model, non-Newtonian fluid rheology, leak-off and reaction kinetics, and adaptive time-stepping provides a robust and field-applicable workflow for acid fracture design optimization in mechanically heterogeneous carbonate reservoirs.
However, several limitations should be acknowledged when interpreting these results. First, uncertainty exists in the conversion of dynamic to static elastic moduli, which may affect the accuracy of in-situ stress estimation. Second, the acid reaction model assumes homogeneous reaction along the fracture, whereas in reality reaction kinetics are heterogeneous and strongly coupled with local flow velocity and temperature. Third, limited well data availability constrains full stress calibration across all layers, introducing potential bias in local stress contrast predictions. Despite these limitations, the integrated framework offers a significant step forward compared to conventional uncoupled approaches, provided that field applications incorporate sensitivity analyses addressing these uncertainties.

8. Conclusion

- In this study, a comprehensive and fully coupled numerical workflow was developed and implemented to simulate hydraulic fracturing treatments under field-representative conditions, specifically for acid fracturing in carbonate reservoirs. Using the GOHFER software platform, the model successfully integrated wellbore geometry, reservoir geomechanical properties, non-Newtonian fluid rheology, time-dependent leak-off mechanisms, and operational pumping schedules within an adaptive time-stepping framework.

- Among the evaluated zones in the Bangestan reservoir (Ilam and Sarvak formations), Zones 6.1 and 6.2 were identified as the most suitable candidates for acid fracturing. This selection was based on a simultaneous evaluation of static and dynamic rock mechanical properties and petrophysical characteristics. In contrast to Zones 4.1, 4.2, and 4.3, which exhibited high elastic moduli, high unconfined compressive strength (UCS), and high brittleness—leading to smooth etched surfaces and poor post-closure conductivity—Zones 6.1 and 6.2 demonstrated significantly lower static and dynamic elastic moduli (below 30 GPa), reduced tensile strength, and a more ductile, semi-brittle mechanical behavior. Petrophysically, Zones 6.1 and 6.2 showed increased oil saturation, a marked reduction in water saturation, and moderate to good reservoir quality (Rank 4 according to EFAC-C classification). Furthermore, the in-situ stress regime within Zones 6.1 and 6.2 was characterized by decreasing fracture initiation pressure gradients (FCP), indicating favorable borehole stability and controlled fracture propagation. Zones 4.1–4.3, despite the presence of oil saturation, exhibited poor reservoir quality (Rank 2–3) and high mechanical stiffness, making them unsuitable for acid fracturing. Zone 5 was excluded due to the risk of vertical fracture growth into adjacent water-bearing layers, and Zone 7 (the saline aquifer) was avoided to prevent water production. Therefore,

the integrated static-dynamic-petrophysical evaluation confirmed that Zones 6.1 and 6.2 represent the optimum target for acid fracturing stimulation.

- Sensitivity analyses performed on injection rate and injected fluid volume revealed strongly nonlinear relationships with fracture geometry. Fracture width increased with injection rate up to an optimum threshold of approximately 22 bbl/min, beyond which further rate increases provided negligible width enhancement. Fracture length exhibited periodic or oscillatory behavior at higher injection rates, with an optimum condition identified at approximately 17 bbl/min. Regarding injected fluid volume, fracture width stabilized beyond 90,000 gal, while maximum fracture length was achieved at approximately 81,000 gal. The observed trade-off between fracture length and height at higher injection volumes, governed by mass conservation and stress redistribution, highlights the necessity of optimizing both parameters simultaneously rather than independently.

- The in-situ stress regime was confirmed as a normal faulting system (Sv > SH > Sh), where the minimum horizontal stress (Sh) primarily controls fracture opening and lateral propagation. The simulation results demonstrated that relatively small variations in Sh significantly alter fracture containment and vertical growth. Increased Sh reduced fracture height growth and promoted lateral extension, whereas decreased Sh allowed greater vertical propagation into adjacent layers. This finding underscores the critical importance of accurate stress calibration for reliable fracture design in layered carbonate systems such as Bangestan.

- Young's modulus (5 MMpsi) and Poisson's ratio (0.25) were identified as key mechanical parameters directly influencing fracture width development and net pressure response. Higher rock stiffness resulted in narrower fractures and elevated net pressure, while lower stiffness promoted wider apertures under identical injection conditions. Since etched fracture conductivity in acid fracturing strongly depends on effective fracture width prior to closure, uncertainties in elastic parameters translate directly into uncertainties in post-treatment productivity. This finding emphasizes the necessity of static-dynamic modulus conversion and core-based calibration in heterogeneous carbonate formations.

- The leak-off coefficient and the fraction of acid reacting before leak-off played a dominant role in controlling fracture extension and effective acid penetration. In low-permeability carbonate layers (k = 0.45 md), leak-off was moderate, allowing sufficient fracture growth while maintaining acid-rock interaction. The simulation confirmed that an optimal balance must be achieved between fracture extension and acid reactivity, as excessive leak-off reduces effective fracture half-length, whereas insufficient leak-off limits acid penetration into the formation matrix.

- The simulated breakdown pressure of approximately 10,800 psi reflects the formation's mechanical resistance. In perforated completions, an additional pressure drop of 5,000–6,000 psi due to perforation friction and near-wellbore tortuosity must be considered. Pressure distribution maps revealed non-uniform net pressure along the fracture plane, directly influencing local aperture variations and explaining the heterogeneous fracture width patterns observed in the simulation. Such heterogeneity is particularly critical in acid fracturing because local aperture variations strongly affect acid transport, diffusion, and dissolution kinetics.

- The fracture length increased steadily until approximately 32 minutes, after which growth stabilized despite continued pumping, indicating a transition toward leak-off-dominated conditions and stress equilibrium. Fracture height exhibited two distinct growth regimes: rapid vertical expansion during the first 15 minutes, followed by a reduced growth rate during the later 40 minutes. This demonstrates that early-time propagation is controlled primarily by injection rate and stress contrast, whereas later growth becomes constrained by mechanical layering and pressure redistribution. Fracture width evolved gradually, ultimately reaching approximately 0.1 inches, a magnitude critical for acid fracturing since etched conductivity is directly proportional to initial fracture aperture and subsequent surface roughness after dissolution.

- The nodal analysis performed using PIPESIM demonstrated that increasing the tubing internal diameter from 2.5 inches to 6 inches improved liquid production capacity by approximately 60–70%, primarily due to reduction in frictional pressure losses along the 3,865-meter vertical flow path. The operating point for the 6-inch tubing configuration reached approximately 1,000–1,050 STB/d at a nodal pressure of about 3,840 psia. Furthermore, the sensitivity analysis on fracture permeability showed that increasing fracture permeability from 10,000 md to 50,000 md raised the production rate from approximately 450 STB/d to 900 STB/d, while bottomhole pressure decreased only slightly. These results confirm that for the studied reservoir, wellbore hydraulics rather than reservoir inflow performance is the dominant factor limiting overall production.

- The fully coupled modeling framework proved essential for capturing stress redistribution around the propagating fracture. As the fracture propagates, local stresses are altered, subsequently affecting growth direction and containment. Simplified uncoupled models would not adequately reproduce these dynamic interactions. The integration of well geometry, calibrated stress model, non-Newtonian fluid rheology, leak-off and reaction kinetics, and adaptive time-stepping provided a robust and field-applicable workflow for acid fracture design optimization in mechanically heterogeneous carbonate reservoirs.

Several limitations should be acknowledged. Uncertainty exists in the conversion of dynamic to static elastic moduli, which may affect the accuracy of in-situ stress estimation. The acid reaction model assumed homogeneous reaction along the fracture, whereas in reality, reaction kinetics are heterogeneous and strongly coupled with local flow velocity and temperature. Limited well data availability constrains full stress calibration across all layers, introducing potential bias in local stress contrast predictions. Despite these limitations, the integrated framework offers a significant advancement compared to conventional uncoupled approaches, provided that field applications incorporate extensive sensitivity analyses addressing these uncertainties. Future work should focus on incorporating thermal effects more rigorously, calibrating reaction kinetics using core-flood experiments, and validating model predictions with post-treatment production data and microseismic monitoring.

Nomenclatures

Latin letters

(σ_c)	Closure Stress, (Psi)
(ρ_{Rock})	Formation Rock Density, (kg/m^3)
(f_r)	Fraction of acid to react before leaking off
(p_f)	Fracturing Pressure, (Psi)
(C_g)	Gas Compressibility, (Psi^{-1})
(γ_g)	Gas Specific Gravity
(H)	Layer Thickness, (m)
(C_o)	Oil Compressibility, (Psi^{-1})
(γ_o)	Oil Specific Gravity
(k)	Permeability
(p_r)	Reservoir Pressure, (Psi)
(T)	Reservoir Temperature, (°F)
(S_p)	Spurt loss, (m)
(C_t)	Total compressibility, (Psi^{-1})
(C_w)	Water Compressibility, (Psi^{-1})
(γ_w)	Water Specific Gravity
(E)	Young's Modulus, (MMPsi)

References

Adachi J, E Siebrits, A Peirce, and J Desroches (2007) Computer Simulation of Hydraulic Fractures. International Journal of Rock Mechanics and Mining Sciences 44(5): 739–757. https://doi.org/10.1016/j.ijrmms.2006.11.006

Albayrak E, and YC Erensal (2004) Using analytic hierarchy process (AHP) to improve human performance: an application of multiple criteria decision making problem. Journal of Intelligent Manufacturing 15(4): 491–503. https://doi.org/10.1023/B:JIMS.0000034112.00652.4c

Alvarez D, J Torres, and L Mendoza (2024) Hybrid Discrete Continuum Modeling of Hydraulic Fracture Interaction. Rock Mechanics and Rock Engineering 57: 1345–1362. https://doi.org/10.1007/s00603-024-02945-1

Amiri H, A Ramezanzadeh, M Chamanzad et al. (2021) Recognizing the best intervals for hydraulic fracturing using a new fracability index. Journal of Petroleum Exploration and Production Technology 11: 3193–3201. https://doi.org/10.1007/s13202-021-01173-7

Anderson M, D Johnson, and P Williams (2014) Laboratory Leak-Off Behavior in Ultra-Tight Formations. SPE Journal 19(4): 612–623. https://doi.org/10.2118/163845-PA

Badri MA (2001) A combined AHP-GP model for quality control systems. International Journal of Production Economics 72(1): 27–40. https://doi.org/10.1016/S0925-5273(00)00077-3

Brown T, M Wilson, and J Garcia (2019) Production Data Analysis from Optimized Multi-Stage Fracturing. SPE Production & Operations 34(3): 512–525. https://doi.org/10.2118/194345-PA

Clark PE (1992) Transport of Proppant in Hydraulic Fractures. SPE Production Engineering 7(2): 177–184. https://doi.org/10.2118/14459-PA

Cleary MP (1978) Hydraulic Fracture Theory: Experimental and Analytical Investigations. International Journal of Rock Mechanics and Mining Sciences 15(1): 23–29.

Crouch SL, and AM Starfield (1990) Boundary Element Methods in Solid Mechanics. Allen & Unwin, London.

Daneshy AA (1973) Mechanics and Direction of Hydraulic Fracturing. Journal of Petroleum Technology 25(1): 111–121. https://doi.org/10.2118/3789-PA

Daneshy AA (1998) Hydraulic Fracture Containment in Layered Formations. SPE Production & Facilities 13(2): 122–130. https://doi.org/10.2118/38301-PA

Detournay E (2007) Propagation Regimes of Fluid Driven Fractures in Impermeable Rocks. International Journal of Geomechanics 7(2): 143–150. https://doi.org/10.1061/(ASCE)1532-3641(2007)7:2(143)

Economides MJ, and KG Nolte (1984) Reservoir Stimulation. Prentice Hall, Englewood Cliffs, NJ.

Economides MJ, AD Hill, and C Ehlig-Economides (2008) Petroleum Production Systems, 2nd ed. Prentice Hall, Upper Saddle River, NJ.

Evans R, R Barree, and M Conway (2013) Slickwater Fracturing and Proppant Transport Efficiency. SPE Production & Operations 28(2): 111–120. https://doi.org/10.2118/159312-PA

Fisher K, N Warpinski, C Wright, and L Davidson (2011) Integrating Geomechanics and Reservoir Simulation. SPE Production & Operations 26(4): 321–332. https://doi.org/10.2118/132345-PA

Garcia L, M Thompson, and R Peterson (2022) Stress Dependent Fracture Conductivity Under Cyclic Loading. Rock Mechanics and Rock Engineering 55(7): 4123–4138. https://doi.org/10.1007/s00603-022-02758-2

Gupta DVS, CS Rai, and RJ Aguilera (2010) Fracture Conductivity and Long Term Production Behavior. SPE Production & Operations 25(1): 87–95. https://doi.org/10.2118/132345-PA

Hassan M, D Zhu, and AD Hill (2020) Coupled Modeling of Acid Fracture Propagation in Carbonate Formations. SPE Journal 25(4): 1785–1798. https://doi.org/10.2118/202354-PA

Huang J, X Zhang, and Y Chen (2014) Thermo Hydro Mechanical Modeling of Hydraulic Fracturing. Journal of Petroleum Science and Engineering 115: 1–12. https://doi.org/10.1016/j.petrol.2013.12.025

Jackson R, AD Hill, and D Zhu (2017) Refracturing in Unconventional Reservoirs. SPE Production & Operations 32(4): 475–486. https://doi.org/10.2118/179138-PA

Kim K, J Park, and S Lee (2019) Microseismic Mapping of Complex Fracture Networks. Geophysics 84(5): KS21–KS34. https://doi.org/10.1190/geo2018-0731.1

Kumar A, P Singh, and R Sharma (2023) Temperature Sensitive Rheology of Crosslinked Gels in High Temperature Reservoirs. Journal of Petroleum Science and Engineering 221: 111123. https://doi.org/10.1016/j.petrol.2023.111123

Lee H, J Morris, and K Slater (2016) Rough Fracture Surface Effects on Residual Aperture. Rock Mechanics and Rock Engineering 49(2): 321–336. https://doi.org/10.1007/s00603-015-0865-3

Lopez R, F Morales, and J Sanchez (2020) Perforation Phasing Effects on Hydraulic Fracture Initiation. SPE Production & Operations 35(3): 522–534. https://doi.org/10.2118/201234-PA

Mahmoud MA, S Elkatatny, and A Abdulraheem (2016) Mineralogical Influence on Fracture Toughness in Shale Formations. Journal of Natural Gas Science and Engineering 34: 1000–1012. https://doi.org/10.1016/j.jngse.2016.08.004

Maxwell SC, J Rutledge, R Jones, and M Fehler (2009) Petroleum Reservoir Characterization Using Downhole Microseismic Monitoring. Geophysics 74(6): WC15–WC26. https://doi.org/10.1190/1.3238361

Mirhashemi M, K Ahangari, AN Dehghan, and K Goshtasbi (2023) Development of a 3D Numerical Modelling to Describe the Conductivity of Acid Fracturing Treatment. NSG2023 29th European Meeting of Environmental and Engineering Geophysics, Vol. 1. European Association of Geoscientists & Engineers, Utrecht. https://doi.org/10.3997/2214-4609.202320078

Morales F, and Y Chen (2025) Artificial Intelligence Assisted Hydraulic Fracture Matching. SPE Production & Operations 40(1): 88–102. https://doi.org/10.2118/219875-PA

Nordgren RP (1972) Propagation of a Vertical Hydraulic Fracture. SPE Journal 12(4): 306–314. https://doi.org/10.2118/3009-PA

Nouri A, M Rezaei, and H Moradi (2018) Experimental Study of Proppant Settling in Shear Thinning Fluids. Journal of Petroleum Science and Engineering 166: 123–134. https://doi.org/10.1016/j.petrol.2018.02.021

Penny GS (1994) Fracture Conductivity: Effects of Closure Stress and Proppant Degradation. SPE Formation Evaluation 9(3): 151–157. https://doi.org/10.2118/20635-PA

Perkins TK, and LR Kern (1970) Widths of Hydraulic Fractures. Journal of Petroleum Technology 22(8): 937–949. https://doi.org/10.2118/89-PA

Peterson R, L Garcia, and M Thompson (2021) Proppant Crushing Under Ultra High Closure Stress Conditions. SPE Journal 26(4): 2150–2163. https://doi.org/10.2118/207195-PA

Rahman S, D Gupta, and M Ali (2024) DFIT Based Calibration of Geomechanical Parameters. SPE Journal 29(3): 1102–1118. https://doi.org/10.2118/217489-PA

Renshaw CE, and DD Pollard (2004) Numerical Simulation of Fracture Propagation in Naturally Fractured Rock. Journal of Geophysical Research 109: B06203. https://doi.org/10.1029/2003JB002785

Rickman R, M Mullen, E Petre, B Grieser, and D Kundert (2011) Practical Use of Shale Petrophysics for Stimulation Design Optimization. SPE Production & Operations 26(4): 357–369. https://doi.org/10.2118/132345-PA

Roberts B, S Maxwell, and T Jones (2015) Zipper Fracturing and Interwell Stress Interaction. SPE Production & Operations 30(3): 223–234. https://doi.org/10.2118/168641-PA

Settari A, and MP Cleary (2006) Development and Comparison of Pseudo 3D and Planar 3D Hydraulic Fracture Models. Journal of Petroleum Science and Engineering 54(1-2): 1–17. https://doi.org/10.1016/j.petrol.2006.06.003

Shah SN (1993) Proppant Settling in Non Newtonian Fluids. SPE Production & Facilities 8(2): 123–130. https://doi.org/10.2118/19891-PA

Silva M, A Teixeira, and P Costa (2018) Hydraulic Fracture Height Growth in Stratified Formations. Rock Mechanics and Rock Engineering 51(5): 1453–1467. https://doi.org/10.1007/s00603-017-1389-8

Singh V, R Patel, and A Kumar (2025) Optimization of Stage Spacing in Horizontal Wells. Journal of Natural Gas Science and Engineering 125: 104567. https://doi.org/10.1016/j.jngse.2024.104567

Thompson M, and H Li (2023) Comparative Modeling of Planar and Complex Hydraulic Fracture Networks. SPE Journal 28(3): 905–921. https://doi.org/10.2118/214586-PA

Valkó P, and MJ Economides (1999) Hydraulic Fracture Mechanics. Wiley, Chichester.

Wang Y, X Li, and Z Chen (2021) Numerical Investigation of Non Darcy Flow in Hydraulic Fractures. Journal of Natural Gas Science and Engineering 89: 103875. https://doi.org/10.1016/j.jngse.2021.103875

Warpinski NR, RA Schmidt, and RJ Northrop (1982) In-Situ Stress: The Predominant Influence on Hydraulic Fracture Containment. Journal of Petroleum Technology 34(3): 653–664. https://doi.org/10.2118/8935-PA

Warpinski NR, MJ Mayerhofer, MC Vincent, CL Cipolla, and EP Lolon (2009) Stimulating Unconventional Reservoirs. Journal of Canadian Petroleum Technology 48(10): 39–51. https://doi.org/10.2118/114160-PA

Williams B, B McDaniel, and T Olson (2012) Stress Shadow Effects in Multi Stage Hydraulic Fracturing. SPE Production & Operations 27(3): 285–294. https://doi.org/10.2118/143385-PA

Yousef A, and T Ahmed (2022) Three Dimensional Proppant Transport Modeling in Hydraulic Fractures. Journal of Petroleum Science and Engineering 208: 109357. https://doi.org/10.1016/j.petrol.2021.109357